Neurobiology of Disease 226 (2026) 107461

Contents lists available at ScienceDirect

Neurobiology of Disease

journal homepage: www.elsevier.com/locate/ynbdi

Ex vivo T2*-weighted MRI and quantitative susceptibility mapping reflect spatial iron accumulation observed on histology in frontotemporal lobar degeneration

Fieke A.M. Prinse [a,b], Elise G.P. Dopper [a], Lucia A.A. Giannini [a], Marjolein Bulk [a], Ernst Suidgeest [b,c], Kyra Dijkstra [d], Renee van Buuren [a], Jelle J. Goeman [e], Niels Dekker [f], Marius Staring [f], Chloé Najac [b], John C. van Swieten [a], Harro Seelaar [a,1], Louise van der Weerd [b,g,*,1]

[a] Department of Neurology, Erasmus University Medical Center, Rotterdam, the Netherlands
[b] C.J. Gorter MRI Center, Department of Radiology, Leiden University Medical Center, Leiden, the Netherlands
[c] Central Animal Facility, Leiden University Medical Center, Leiden, the Netherlands
[d] Department of Pathology, Leiden University Medical Center, Leiden, the Netherlands
[e] Department of Biomedical Data Sciences, Leiden University Medical Center, the Netherlands
[f] Division of Image Processing, Department of Radiology, Leiden University Medical Center, Leiden, the Netherlands
[g] Department of Human Genetics, Leiden University Medical Center, Leiden, the Netherlands

ARTICLE INFO

Keywords:
Frontotemporal lobar degeneration
Ex vivo
Iron
Quantitative susceptibility mapping
T2*-weighted MRI
Histology

ABSTRACT

Iron accumulation is known to be involved in frontotemporal lobar degeneration (FTLD) and possibly with a different spatial pattern in FTLD with tau (FTLD-tau) versus TDP-43 (FTLD-TDP) pathology. In this study, we aimed to visualize the spatial distribution of iron in ex vivo brain tissue with FTLD and healthy controls using both histology and MRI. High resolution multi-echo T2*-weighted 7T MRI was performed on ex vivo tissue of the frontal and temporal cortex of 14 FTLD cases (6 FTLD-tau, 8 FTLD-TDP) and 11 healthy controls (HC) to obtain T2*-weighted images and quantitative susceptibility maps (QSM). These tissue blocks were then stained for iron. The spatial iron distribution was assessed visually by different scoring features on the three modalities (T2*-weighted MRI, QSM, and histology) and analyzing cortical layer profiles of the signal intensity. We found more iron accumulation in the temporal cortex of FTLD cases compared to HC, displayed by higher visual ratings and lower signal intensity values on cortical layer profiles. Histology showed a good correlation with T2*-weighted MRI. QSM offered complementary information compared to T2*-weighted MRI, particularly for identifying distinct histological features of iron accumulation within the subcortical U-fibers. We conclude that iron accumulation is involved in the disease process of FTLD and that T2*-weighted MRI and QSM can be used as a noninvasive imaging modality to study cortical and subcortical iron accumulation in FTLD.

1. Introduction

Frontotemporal lobar degeneration (FTLD) is the second most common cause of early onset dementia, clinically presenting as behavioral variant frontotemporal dementia (bvFTD) with behavioral impairments, primary progressive aphasia (PPA) with language difficulties, and/or progressive supranuclear palsy (PSP) or corticobasal syndrome (CBS) with motor disturbances. FTLD is characterized by atrophy in the frontal and/or temporal lobes and accumulation of aggregated proteins. In 95% of the cases, patients have either accumulation of TDP-43 (FTLD-TDP) or tau (FTLD-tau) (Grossman et al., 2023). Most cases of FTLD are sporadic, but ~30% of the cases have a genetic cause with mutations in *microtubule associated protein tau* (*MAPT*) (Hutton et al., 1998) or *progranulin* (*GRN*) (Baker et al., 2006; Cruts et al., 2006) and the *chromosome 9 open reading frame 72* hexanucleotide repeat expansion (*C9orf72*-HRE) (DeJesus-Hernandez et al., 2011; Renton et al., 2011) as most common

* Corresponding author at: C.J. Gorter MRI Center, Department of Radiology, Leiden University Medical Center, Leiden, the Netherlands.
E-mail address: l.van_der_weerd@lumc.nl (L. van der Weerd).
[1] These authors contributed equally.

https://doi.org/10.1016/j.nbd.2026.107461
Received 18 March 2026; Received in revised form 22 May 2026; Accepted 26 May 2026
Available online 27 May 2026
0969-9961/© 2026 The Authors. Published by Elsevier Inc. This is an open access article under the CC BY license (http://creativecommons.org/licenses/by/4.0/).

genetic causes.

Iron is present in the brain for various processes such as myelin production, proliferation, and mitochondrial functioning (Ferretti and Zanella, 2024). Although iron accumulation increases during healthy aging, several neurodegenerative diseases, such as Alzheimer's Disease (AD), amyotrophic lateral sclerosis (ALS), and Parkinson's Disease (PD), have shown dysregulation of the iron homeostasis (Ayton et al., 2025; Dusek et al., 2022). This pathological iron accumulation occurs through several mechanisms like mitochondrial dysfunction, protein misfolding and aggregation, or neuroinflammation, may contribute to neuronal loss. In progressive supranuclear palsy (PSP), a pathological subtype of FTLD-tau, iron stored as ferritin, co-localized with tau filaments, particularly in glial cells (Pérez et al., 1998), and astrocytes (Lee et al., 2023; Lee et al., 2017). Previously, our group compared iron accumulation patterns in ex vivo FTLD-*MAPT* and FTLD-*C9orf72* cases. The study showed diffuse mid-cortical iron bands and superficial iron bands in both groups in the frontal and temporal cortex, although to a lesser extent in FTLD-*C9orf72*. These patterns of cortical iron accumulation, associated with protein aggregates and neuronal degeneration, correlated with activated and dystrophic microglia and reactive astrocytes. Additionally, a pilot study with a small number of cases used ultra-high field T2*-weighted (T2*-w) MRI and showed good correspondence between hypointense changes on MRI and cortical iron observed on histology (Giannini et al., 2023).

Iron-sensitive MRI techniques, such as T2*-w imaging, susceptibility weighted imaging (SWI), and quantitative susceptibility mapping (QSM) are noninvasive methods for detecting iron accumulation in disease. Increased iron levels in multiple cortical and subcortical brain regions of sporadic FTLD, positively correlated with clinical variables, like apathy, behavioral traits, and disinhibition (Mazzucchi et al., 2019; Sheelakumari et al., 2017) in several studies in FTLD. In addition, more iron accumulation was shown in the subcortical regions of patients with PSP or CBS with probable underlying FTLD-tau compared to healthy controls (HC) (Satoh et al., 2023).

Ex vivo MRI offers the unique advantage of enabling higher resolution imaging, facilitating precise visualization of iron deposits in specific brain regions and direct comparison with histology. Few studies have investigated iron content in brain tissue of FTLD cases. So far, two FTLD studies have reported increased iron content visible on T2*-w MRI in various regions of the brain, e.g., the (sub)thalamus, the basal ganglia, and frontal and temporal cortex (De Reuck et al., 2017; De Reuck et al., 2014). By correlating histopathology and T2*-w and SWI MRI in FTLD, spatial differences in iron accumulation were observed between FTLD-TDP and FTLD-tau (Tisdall et al., 2022), making iron accumulation a potential biomarker to differentiate between FTLD-TDP and FTLD-tau. However, SWI or T2*-w MRI cannot provide quantitative information on iron content, as the resulting contrast reflects a mixture of paramagnetic and diamagnetic sources that cannot be disentangled. QSM has the potential to both quantify and precisely localize iron (Langkammer et al., 2018), and was shown to correlate well with histologically confirmed iron accumulation in AD (Bulk et al., 2020) but has not been studied in FTLD to date.

The primary aim of this study was to systematically compare the sensitivity of ex vivo ultra-high field (7T) T2*-w MRI and QSM to iron histology for detecting layer-specific iron accumulation in FTLD, and to assess whether these MRI modalities can distinguish FTLD from HC. To this aim, we directly compared MRI and histology using both visual rating scores and quantitative cortical layer profiles. We hypothesized a good correlation for the depiction of iron accumulation across the three modalities and more pathological iron accumulation in FTLD cases compared to HC.

2. Methods

2.1. Postmortem brain material

Formalin-fixed tissue from the right hemisphere of 14 FTLD cases and 11 HC were included. Depending on the tissue availability, the middle frontal gyrus and the middle temporal cortex or the temporal pole were included. Fig. 1 shows an overview of the study. All material was obtained through the Netherlands Brain Bank. Autopsy was carried out according to the Legal and Ethical Code of Conduct of the Netherlands Brain Bank. Anonymity of all subjects was preserved by using a de-identified system for the tissue samples following Dutch ethical guidelines (Code for Proper Secondary Use of Human Tissue and Dutch Federation of Medical Scientific Societies). Informed consent was obtained before death.

2.2. MRI – T_2*-weighted MRI

The tissue was scanned on a 7T PharmaScan Bruker MRI system with a 38 mm transmit-receive volume coil and ParaVision 360 imaging software for the FTLD cases and ParaVision 5.1 imaging software for the HC (Bruker BioSpin, Ettlingen, Germany). 3D Multiple gradient echo (MGE) scans with a total scan time of 10 h were acquired. The following scan parameters were used for the FTLD cases: 9 echoes, TE_1:ΔTE:TE_{max} = 3.5:5:43.5 ms, TR = 150 ms, flip angle = 25° at 100 μm isotropic resolution. The field of view (FOV) was 3 × 3 × 1.3 cm and an acquisition matrix of 300 × 300 × 130 with a coronal slice orientation, and a bandwidth of 75,757.6 Hz. The HC were scanned with slightly different parameters: 4 echoes, TE_1:ΔTE:TE_{max} = 12.5:10.7:44.6 ms, TR = 75.0 ms, flip angle = 25° at 100 μm isotropic resolution. The FOV was 2.4 × 1.4 × 1.2 cm and an acquisition matrix of 240 × 140 × 120 with a coronal scan orientation, and a bandwidth of 25,000 Hz.

T2*-w MRI data of six cases (four FTLD-tau, two FTLD-TDP) were also included in a previous pilot study of our group (Giannini et al., 2023).

2.3. MRI - quantitative susceptibility mapping

QSM maps were reconstructed from the 3D MGE scans using the SEPIA toolbox (v1.2) for QSM data (Chan and Marques, 2021). First, the Brain Extraction Tool (BET) was used on the magnitude data to isolate the tissue block (f = 0.3) (Smith, 2002). We used Optimum weights Laplacian (MEDI toolbox, Medimagemetric LLC, Jan 2020) for phase unwrapping and echo phase combination (Robinson et al., 2017; Schofield and Zhu, 2003), VSHARP (v3.0) for background field removal, with a spherical harmonic of the second order as refine method and a radius of [10:-1:1] (Li et al., 2011), and MEDI (MEDI toolbox, Medimagemetric LLC, Jan 2020) for the dipole inversion (Liu et al., 2012; Liu et al., 2011; Liu et al., 2018), all as implemented in SEPIA. No reference tissue was used as there was no cerebrospinal fluid (CSF) and the ratio between white matter and gray matter was not consistent for the cases. QSM figures are presented with Chi range [−0.065 0.065]. One control had no QSM data for the frontal cortex due to failed reconstruction.

2.4. Histology

After the MRI, tissues were embedded in formalin-fixed paraffin. 20 μm sections were cut and stained using an in-house developed DAB-enhanced Prussian Blue protocol (van Duijn et al., 2011). This staining method is thought to aspecifically stain both the ferric and ferrous state of non-heme iron. The slides were digitized using an automatic bright field microscope (Philips Ultra Fast Scanner, Philips, Netherlands) for microscopic evaluation with a 0.25 μm resolution. The intensity range of the histological slides was then manually adjusted to account for experimental variations in staining intensity. Briefly, the maximum value was determined by the maximum pixel intensity in the

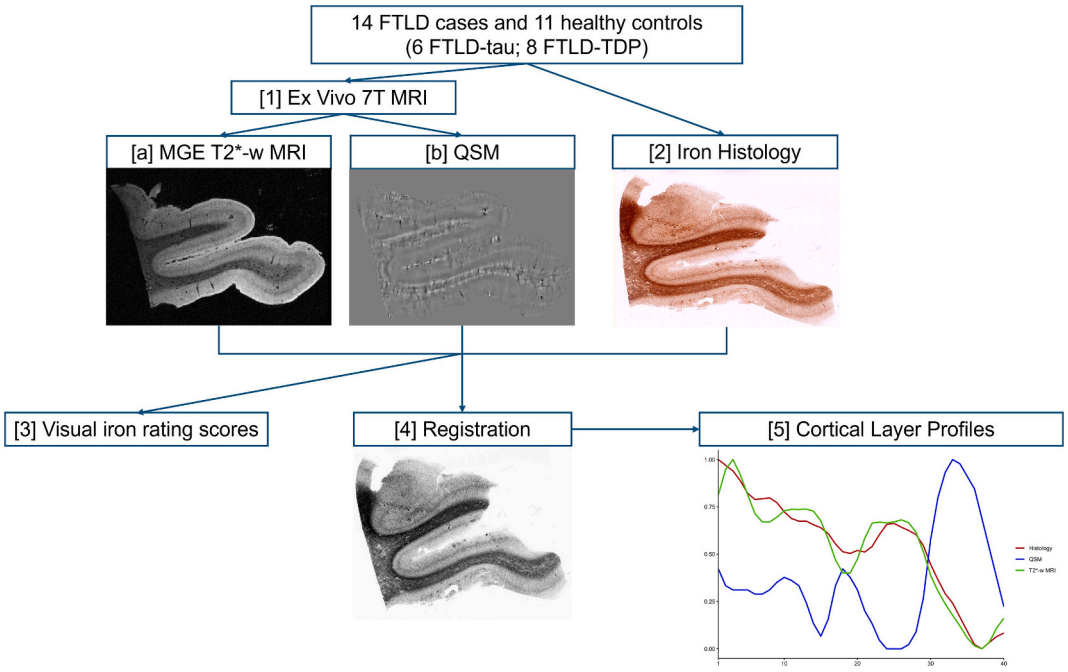

Fig. 1. Overview of the study. 14 FTLD cases and 11 healthy controls were included. All cases were first scanned on the 7 T Bruker MRI system [1] to acquire T2*-w magnitude images [a] and QSM maps [b]. Then, the tissue blocks were embedded and stained for histological data [2]. All three data types were scored visually for iron on several criteria [3]. Afterwards, the histological slide was converted to gray scale, down sampled, and registered to the T2*-w magnitude slice and the QSM [4]. Then, signal intensities over the cortical layers and the superficial white matter were extracted and compared between FTLD and HC [5]. QSM is visualized with scale [−0.065:0.065]. FTLD: frontotemporal lobar degeneration; HC: healthy controls; QSM: quantitative susceptibility mapping; Tau: tubulin associated unit; TDP: TAR DNA-binding Protein 43; w: weighted.

background and the minimum value by the average pixel intensity of the deep white matter per case. This resulted for all images in a white background and a similar dark appearance of the white matter.

2.5. Scoring

For each subject, the frontal and temporal cortex were scored for the presence of iron accumulation using previously used categories on all three modalities (T2*-w MRI, QSM, histology) independently (Table 1) (Bulk et al., 2018a; Bulk et al., 2018b; Giannini et al., 2023). Examples of the different scoring criteria for each modality are shown in Fig. 2. The 4D T2*-w magnitude and 3D QSM images were scored on a 2D slice that most closely matched the 2D histological section. Those scores were then checked for consistency across the entire 3D volume. For one case, the given score was not representative for the whole block, thus the score was adjusted to the rating for the entire volume. T2*-w MRI was scored at a TE of 33.5 ms (7th echo) for the FTLD cases and a TE of 33.9 ms (3rd echo) for the HC. All images were scored by two independent experienced raters (FAMP and LvdW) blinded for diagnosis and iron scores for the other modalities. In case of discrepancy between the two raters, the image was reviewed together, and consensus was reached.

Table 1
Scoring features for the visual rating scores for iron accumulation.

Feature	Scoring	Value
Homogeneity of the cortex	Yes (homogeneous)	0
	No (inhomogeneous)	2
Diffuse hypointense mid cortical band	Absent	0
	Partially present	1
	Present	2
Superficial hypointense band	Absent	0
	Partially present	1
	Present	2
U-fibers	Absent	0
	Partially present	1
	Present	2

2.6. Registration histology - MRI

To enable registration of 2D histology to 3D QSM or 4D T2*-w MRI, the most similar slice of the T2*-w magnitude MGE MRI and the generated QSM map compared to the histological image was manually selected based on visual landmarks. The histology slide was then down-sampled by a factor of 400 to more closely match the resolution of the MRI, and colour adjusted to a 32-bit gray image to facilitate registration. The histology slide was registered to the seventh echo for the FTLD cases or the third echo for the HC of the T2*-w magnitude image with affine registration using the ITK-elastix toolbox (Ntatsis, 2023; Shamonin et al., 2013). In cases that were more challenging to register, the translation and rotation components were manually initialized. The registered result was directly transposed on the 2D QSM, as the latter was reconstructed from the T2*-w MGE data.

2.7. Cortical layer profile analysis

To determine the spatial pattern of iron over the cortical layers and the superficial white matter, a signal intensity profile was constructed using FIJI (v. 2.16.0) (Schindelin et al., 2012). A line was manually drawn in the middle of a gyrus and sulcus perpendicular to the white matter, making sure there were no artifacts or other structures (e.g., cortical vessels) present in any of the three modalities. This line was divided into 40 equal segments, with the first segment starting on the outer border of the gray matter. The 30th segment was placed on the border of the gray matter and white matter. The profile extended for a further 10 segments into the white matter. This fixed number of segments allowed us to normalize the cortical profiles for differences in cortical thickness and atrophy between the cases. From the cortical layer profile, gray-level intensity values were extracted and averaged over a 5-pixel (500 μm) linewidth for each modality.

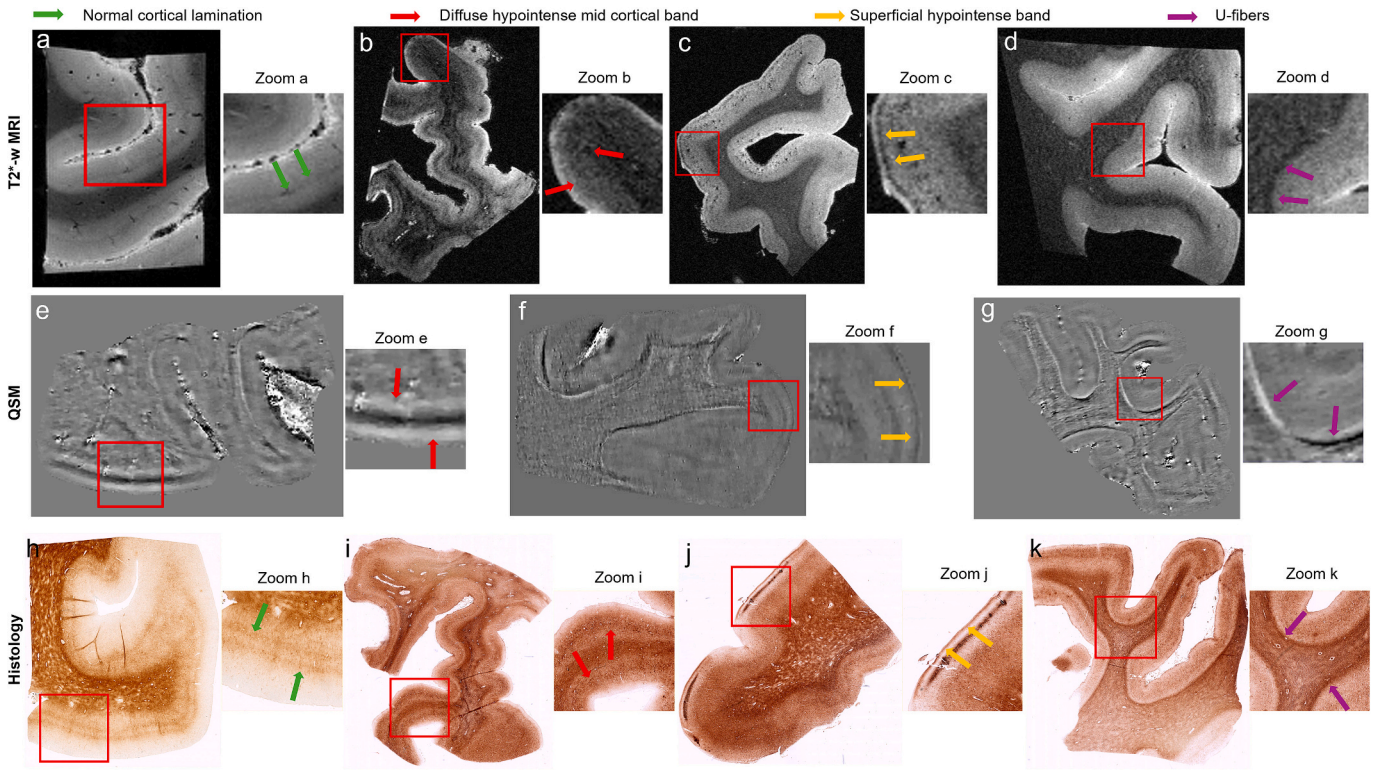

Fig. 2. Scoring examples for the visual rating scores for T2*-w MRI, QSM, and histology. First row depicts T2*-w magnitude MRI (third or seventh echo). Row two are examples of QSM images. Note, homogeneity was not scored on QSM data. Third row are the histological slides. A normal cortex (A, H; green arrows) was defined as a homogeneous appearance with two distinct layers, corresponding to the lines of Baillarger. An abnormal cortex (B, I) had an inhomogeneous appearance and often showed a diffuse hypointense band in the mid cortical layers, obscuring the normal cortical lamination (B, E, I, red arrows). This diffuse band was hypointense on the T2*-w MRI and histology and could be white or black on the QSM depending on the orientation to the main magnetic field. An additional hypointense band could be observed in the superficial cortical layers, the superficial hypointense band (C, F, J, yellow arrows). This superficial hypointense band was black on the T2*-w MRI and histology, but white or black on the QSM. In the superficial white matter, a hypointense band, the U-fibers could be observed on the T2*-w MRI and histology, and white or black on the QSM (D, G, K, purple arrows). Rectangles indicate the location of the zooms. QSM is visualized with scale [−0.065:0.065]. QSM: quantitative susceptibility mapping; T2*-w MRI: T2*-weighted magnetic resonance imaging;. (For interpretation of the references to colour in this figure legend, the reader is referred to the web version of this article.)

To directly compare the signal intensity profiles between subjects and modalities, the extracted values were normalized between 0 and 1. For the cortical layer profiles of the QSM, the values were normalized based on the 1st and 99th percentile of the whole dataset. The 1st percentile was set as 0 and the 99th percentile as 1. Values outside this range were not capped but calculated accordingly. The extracted values for the cortical layer profiles of the histology ranged between 0 and 255. To account for staining intensity differences, we applied the window as described above for every case individually and normalized all datasets between 0 and 1 based on the 1st and 99th percentile of the whole dataset. For the T2*-w data we assumed that the proton density would not be significantly different between subject, and therefore we calculated the signal intensity relatively to the signal intensity of the echo with TE 12.5 ms. To normalize the whole T2*-w dataset, we calculated the 1st and 99th percentile and rescaled the data accordingly.

For the T2*-w MRI and the histological images, a lower normalized signal intensity value corresponded to a darker appearance on the images, reflecting higher iron load. Higher normalized signal intensity values on the QSM corresponded to increased susceptibility (interpreted as higher paramagnetic load, presumably iron). The U-fibers in the superficial white matter can be either white or black, because the diamagnetic myelinated fibers are highly anisotropic and therefore the susceptibility is dependent on their orientation to the magnetic field (Wharton and Bowtell, 2015). One case was excluded for the cortical layer profiles of T2*-w MRI and the QSM due to failed reconstruction.

2.8. Statistical analysis

Demographic characteristics were compared using independent samples *t*-tests for continuous data and chi-square tests for categorical data. To test if there was more iron accumulation in FTLD vs HC, the following analyses were done separately per modality and brain region. The association between the scores of the different features and disease status (FTLD vs control) were first compared using a Cochran Armitage test for Linear Trend, taking FLTD-tau and FTLD-TDP together. Afterwards, if the trend tests were significant, separate Cochran Armitage tests were done for the pairwise comparisons of the subgroups FTLD-tau, FTLD-TDP, and HC. This controls for familywise error rate in the pairwise comparisons through the closure principle (Goeman and Solari, 2022). To test for a potential spatial pattern in these scores, we constructed a heatmap of the visual rating scores. Firstly, the order of the x-axis was determined by the overall score per scorings feature on the histology, i.e., the feature with the highest overall score was placed on the right side, the feature with the lowest overall score on the left side. The y-axis was then ordered based on the overall score per subject on the histology data with the highest score at the top and the lowest at the bottom. The T2*-w and QSM heatmaps were ordered as well with the ranking of the histology data. We then calculated the summability score. Summability is a measure for unidimensionality of the scoring feature (Goeman and De Jong, 2018).

To test if there was a difference in the cortical layer profiles between FTLD and HC, we calculated the mean normalized signal intensity values for the two groups (FTLD and HC) per modality and cortex. We then

calculated the area between these two lines (FTLD and HC) by summation of the square difference between the means. To test whether this calculated area was significantly different, we used a permutation test: we randomly reassigned the labels FTLD or HC and recalculated the test statistic (the area between the curves) with 10^4 such reassignments to acquire a null distribution. The *p*-value of the resulting permutation test was the fraction of reassignment test statistics that was more extreme than the true data value. To test whether the cortical layer profiles of the modalities were similar to each other, a Pearson's correlation coefficient was calculated per case between histology and T2*-w MRI, between histology and QSM, and between T2*-w MRI and QSM. We transformed these correlations using Fisher's z-transform before averaging the for each comparison over all participants. *P*-values for these correlations were calculated with a Fisher's combination method. Statistical significance was set at $p < 0.05$. All statistical analyses were performed using R version 4.3.3 [R Core Team, 2021].

2.9. Supplementary materials and methods

Detailed description of the study design, MRI postmortem tissue preparation, histological staining protocol, and the scoring criteria are provided in Appendix A. Supplementary Materials and Methods.

3. Results

3.1. Demographics

Demographics are given in Table 2. The FTLD cases were significantly younger than the HC ($p < 0.001$). There was no difference in age between FTLD-TDP and FTLD-tau ($p = 0.07$). There was no difference in sex distribution ($p = 0.366$) or postmortem delay ($p = 0.099$) for any of the groups.

3.2. Visual rating scores

All *p*-values of the comparison between FTLD and HC are reported in Table 3. All p-values for the comparison between FTLD-tau, FTLD-TDP, and HC are mentioned in Supplementary Table A.1 (frontal cortex) and A.2 (temporal cortex).

3.2.1. Iron scores on T2*-w MRI

In the temporal cortex, FTLD cases had more often an inhomogeneous cortex ($p = 0.026$) and a diffuse hypointense mid cortical band ($p = 0.011$) compared to HC, but there was no significant difference in the presence of the superficial hypointense band or U-fibers (Fig. 3a). Both FTLD-TDP and FTLD-tau had more often a diffuse hypointense mid cortical band compared to HC ($p = 0.040$; $p = 0.020$). FTLD-tau had more often an inhomogeneous cortex compared to HC ($p = 0.049$) (Supplementary Fig. A.1a). There was no difference between FTLD-tau and FTLD-TDP.

In the frontal cortex, the superficial hypointense band was present more often in the FTLD cases compared to the HC ($p = 0.002$) (Fig. 3b). Both the FTLD-tau and FTLD-TDP cases had this superficial hypointense band more often compared to HC (FTLD-TDP: $p = 0.002$, FTLD-tau: $p = 0.004$), but there was no difference between FTLD-tau and FTLD-TDP (Supplementary Fig. A.1b). There were no differences in scores for the homogeneity of the cortex, diffuse hypointense mid cortical band, or U-fibers in the superficial white matter between FTLD and HC in the frontal cortex.

3.2.2. Iron scores on QSM

In the temporal cortex, the diffuse hypointense mid cortical band and superficial hypointense band were observed more often in FTLD cases compared to HC ($p = 0.003$; $p = 0.002$ respectively) (Fig. 4a). Secondary analysis showed that the superficial hypointense band was observed more often in both FTLD-TDP ($p = 0.009$) and in FTLD-tau ($p = 0.002$) compared to HC, without a difference between FTLD-TDP and FTLD-tau. The presence of the diffuse hypointense mid cortical band was increased in the FTLD-TDP compared to the HC ($p = 0.002$), but not in FTLD-tau (Supplementary Fig. A.2a). There was no difference in the presence of U-fibers.

U-fibers were more frequently detected in the FTLD cases compared to HC in the frontal cortex ($p = 0.004$) (Fig. 4b). Both in FTLD-TDP and FTLD-tau the U-fibers were more prominent compared to the HC ($p = 0.020$; $p = 0.018$, respectively), but there was no difference between FTLD-tau and FTLD-TDP (Supplementary Fig. A.2b). There was no significant difference for the diffuse hypointense mid cortical band or the superficial hypointense band.

Interestingly, we observed some instances where the mid-cortical bands seemed to be orientation-dependent, e.g., in Fig. 2e, indicating that also in the cortex, there was anisotropy of diamagnetic or paramagnetic sources,

3.2.3. Iron scores on histology

In the temporal cortex, an inhomogeneous cortex ($p < 0.001$), a diffuse hypointense mid cortical band ($p < 0.001$), and a superficial

Table 2
Patient characteristics of the cohort.

	FTLD-Tau	FTLD-TDP	HC	P-value
N	6	8	11	
Female (%)	0 (0%)	4 (50%)	6 (55%)	0.365
Male (%)	6 (100%)	4 (50%)	5 (45%)	0.365
Age at death (years)	59.7 ± 11.8	70.5 ± 3.25	80.7 ± 9.3	0.0007*
Postmortem delay (hours)	5.53 ± 0.35	5.98 ± 0.99	6.66 ± 1.49	0.099
Clinical diagnosis				
bvFTD (%)	5 (83%)	4[a] (50%)		
PPA (%)	0	4[a, b] (50%)		
PSP (%)	1 (17%)			
Sporadic	1	4		
Mutation	5	4		
MAPT	5			
C9orf72		2		
GRN		1		
TUBA4A		1		

bvFTD: behavioral variant frontotemporal dementia; *C9orf72:* chromosome 9 open reading frame 72; *GRN:* progranulin; HC: healthy controls; *MAPT*: microtubule associated protein tau; PPA: primary progressive aphasia; PSP: progressive supranuclear palsy; Tau: tubulin associated unit; TDP: TAR DNA-binding protein 43; *TUBA4A*: tubulin alpha 4a.

* $P < 0.05$.

[a] One patient developed amyotrophic lateral sclerosis.

[b] Two patients developed progressive supranuclear palsy/corticobasal syndrome.

Table 3
P-values of the Cochran Armitage test for Trend to compare patient status (FTLD vs HC) and the visual rating score features.

Frontal	Homogeneity	Diffuse hypointense mid cortical band	Superficial hypointense band	U-fibers
T2*-w MRI	0.201	0.895	0.002*	0.283
QSM	NA	0.242	0.481	0.004*
Histology	0.173	0.032*	0.018*	0.008*
Temporal	**Homogeneity**	**Diffuse hypointense mid cortical band**	**Superficial hypointense band**	**U-fibers**
T2*-w MRI	0.026*	0.011*	0.070	0.494
QSM	NA	0.004*	0.002*	0.069
Histology	0.0001*	0.0002*	0.036*	0.596

FTLD: frontotemporal lobar degeneration; HC: healthy controls; QSM: quantitative susceptibility mapping; T2*-w MRI: T2*-weighted magnetic resonance imaging.
* $p < 0.05$.

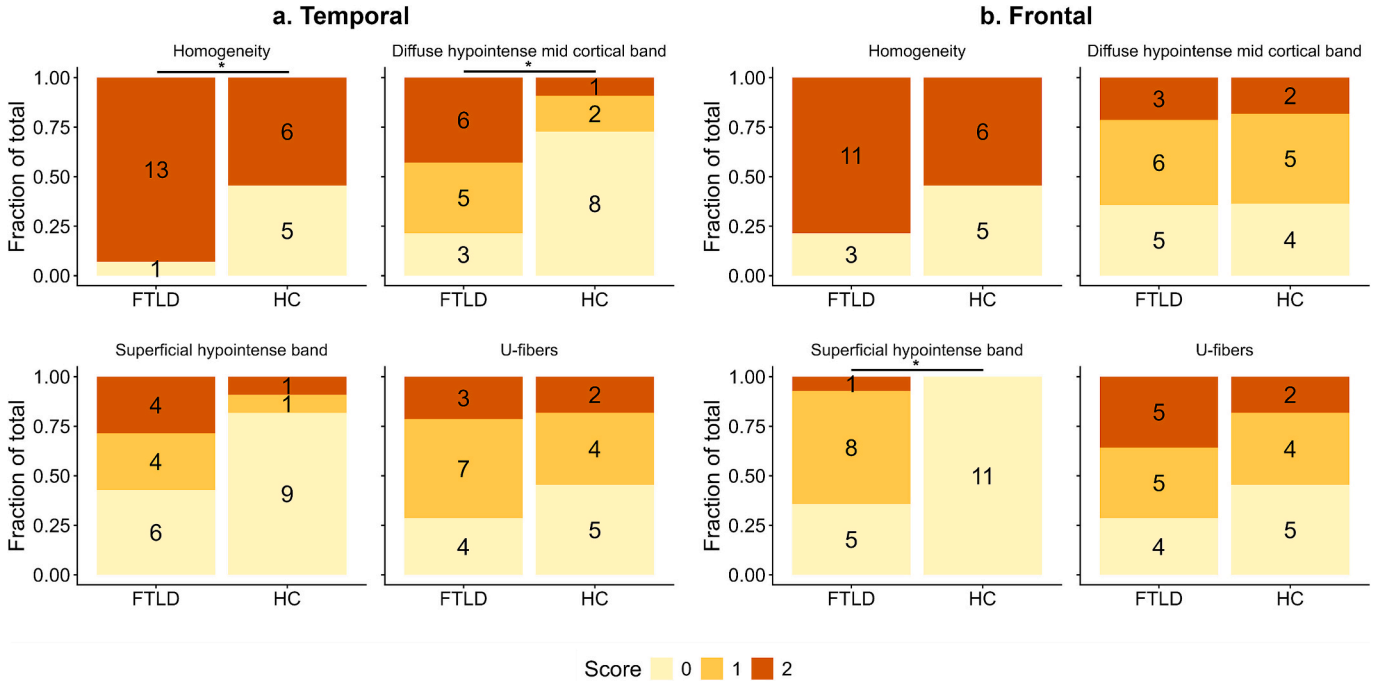

Fig. 3. Boxplots of the frequencies of the visual rating scores for FTLD and HC on all four scoring features on T2*-w MRI. A. The visual rating score frequencies for the temporal cortex. A difference was found in the occurrence of inhomogeneity and the diffuse hypointense mid cortical band for the two groups. B. The visual rating score frequencies for the frontal cortex. A difference was found between the status (FTLD and HC) and the occurrence of the superficial hypointense band. The numbers in the colored sections of the bars represent the observed frequency. * $p < 0.05$. FTLD: frontotemporal lobar degeneration; HC: healthy controls.

hypointense band ($p = 0.036$) were more frequent in FTLD compared to HC (Fig. 5a). Both FTLD-TDP and FTLD-tau had an inhomogeneous cortex ($p = 0.002$; $p = 0.004$), and a diffuse hypointense mid cortical band ($p = 0.001$; $p = 0.005$) more often compared to HC. Only FTLD-TDP cases showed the superficial hypointense band more frequently compared to HC ($p = 0.011$) (Supplementary Fig. A.3a). There was no difference in the presence of U-fibers.

In the frontal cortex, the presence of the diffuse hypointense mid cortical band ($p = 0.032$), the superficial hypointense band ($p = 0.0179$), and the U-fibers ($p = 0.008$) was more prominent in FTLD compared to the HC (Fig. 5b), whereas there was no difference in homogeneity of the cortex. These differences were all found in FTLD-TDP compared to HC (diffuse: $p = 0.011$; superficial: $p = 0.004$; U-fibers: $p = 0.010$), but not in FTLD-tau (Supplementary Fig. A.3b).

3.3. Heatmaps

The heatmaps (Supplementary Fig. A.4) show the variability of the scores and patterns of iron accumulation across the subjects on histology, which we considered as gold standard. The order of the subjects was then maintained for the T2*-w MRI and QSM heatmaps. We did not find any temporal order in the spread of iron across the different features in any of the three modalities. The summability scores were 0.328 for histology, 0.298 for T2*-w MRI, and 0.261 for QSM, indicating a weak or no correlation between the order of the affected visual scoring features and the two groups (FTLD and HC).

3.4. Cortical layer profiles FTLD vs HC

Examples of the chosen slices per modality and their cortical layer profiles of a HC and a FTLD case are shown in Fig. 6. Typically, for the HC the signal intensity values in the cortical layers are higher than in the FTLD cases, with two small dips around segments 10 and 20 reflecting the lines of Baillarger, which are more myelinated and iron rich. There is a steep drop in the signal intensity values around segment 30, marking the gray matter/white matter border. The U-fibers are depicted as a sharp decrease for the QSM, markedly separated from the deeper white matter. On T2*-w MRI and histology, the U-fibers are also visible, but far less distinguishable from the deeper white matter. The FTLD case shows a steep in the first segments, followed by a gradual decrease in signal

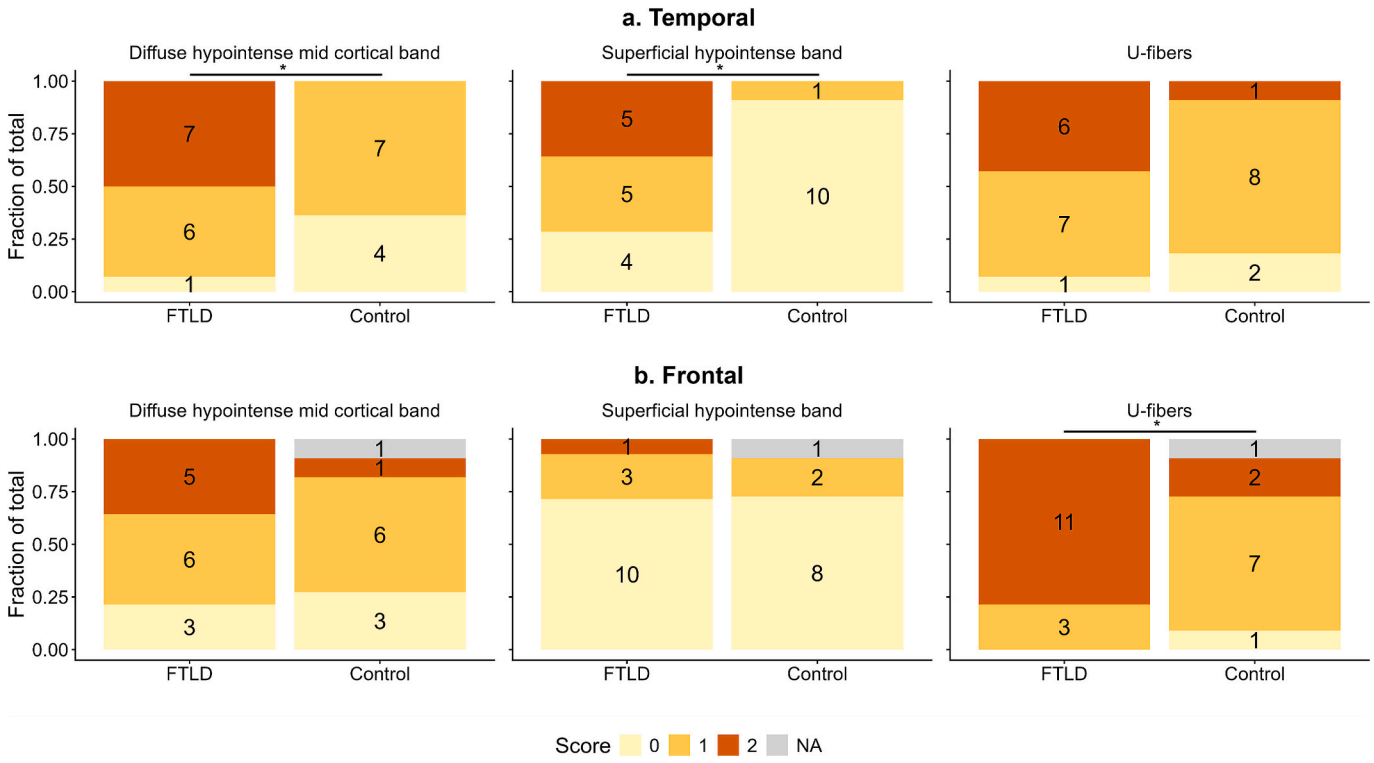

Fig. 4. Boxplots of the frequencies of the visual rating scores for FTLD and HC on all four scoring features on QSM. A. The visual rating score frequencies for the temporal cortex. A difference was found in the occurrence of the diffuse hypointense mid cortical band and the superficial hypointense band for the two groups. B. The visual rating score frequencies for the frontal cortex. A difference was found between the status (FTLD and HC) and the occurrence of U-fibers. The numbers in the colored sections of the bars represent the observed frequency. Note: homogeneity was not scored on the QSM. One dataset for the frontal cortex was missing due to failed reconstruction (NA). * $p < 0.05$. FTLD: frontotemporal lobar degeneration; HC: healthy control.

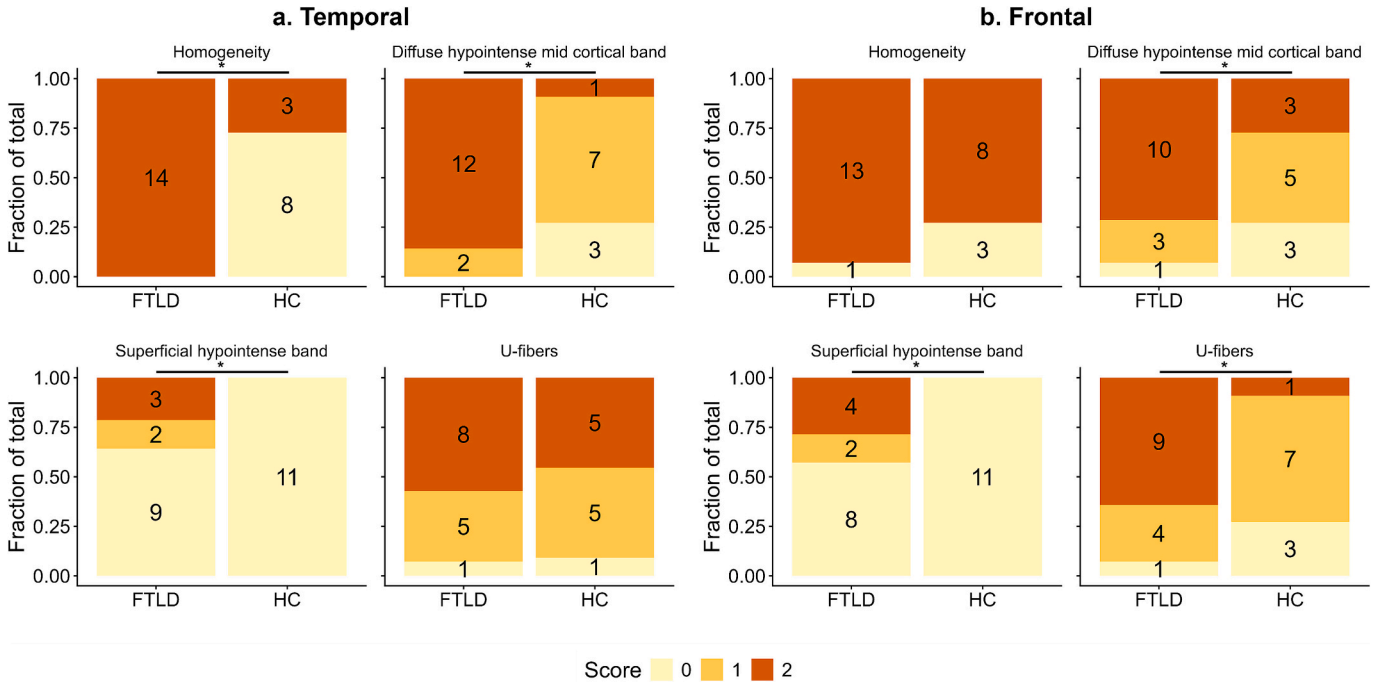

Fig. 5. Boxplots of the frequencies of the visual rating scores for FTLD and HC on all four scoring features on iron histology. A. The visual rating score frequencies for the temporal cortex. A difference was found in the occurrence of inhomogeneity, the diffuse hypointense mid cortical band, and the superficial hypointense band for the two groups. B. The visual rating score frequencies for the frontal cortex. A difference was found between the status (FTLD and HC) and the occurrence of the diffuse hypointense mid cortical band, the superficial hypointense band, and the U-fibers. The numbers in the colored sections of the bars represent the observed frequency. * $p < 0.05$. FTLD: frontotemporal lobar degeneration; HC: healthy controls.

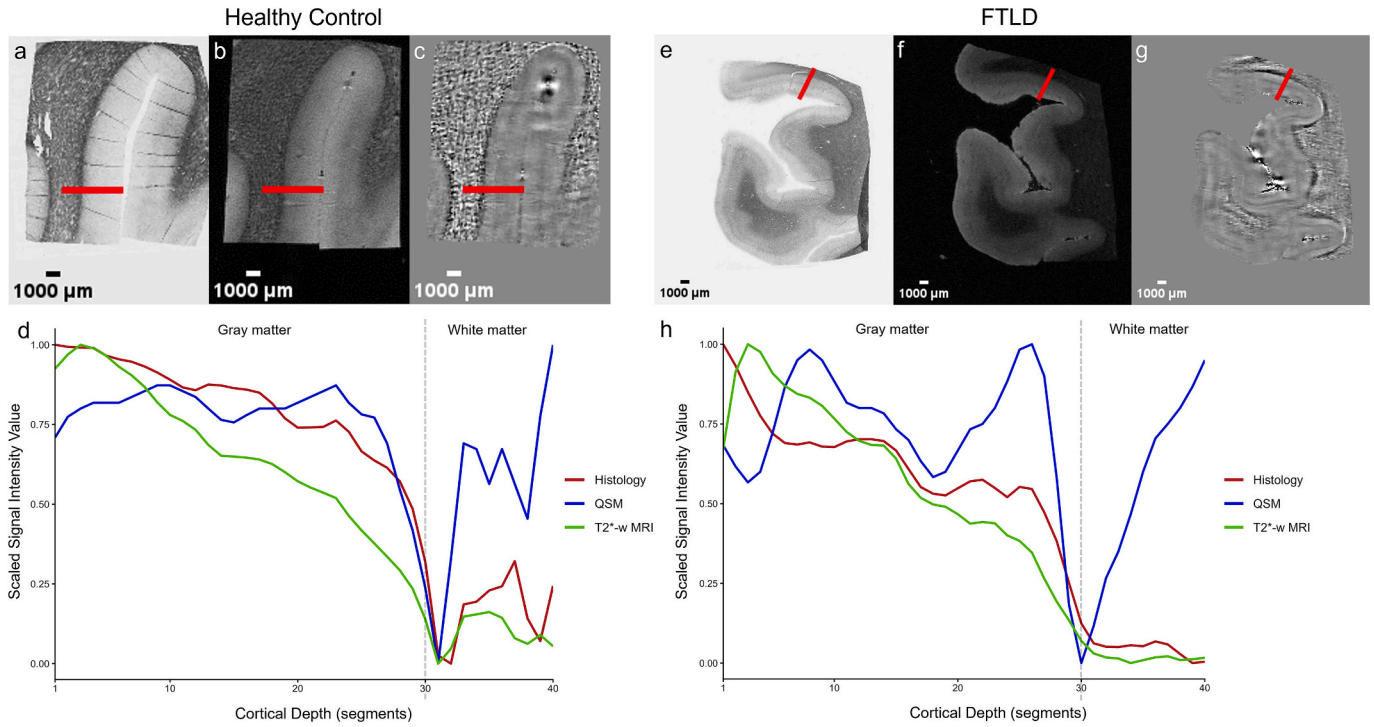

Fig. 6. Example of the registered histology (a, e), T2*-w MRI (b, f), and QSM (c, g) with the location of the line and their respective cortical layer profiles of the signal intensity (d, h) for a healthy control and a FTLD case. Red line depicts the location of the cortical layer profile. Point 1 is the gray matter/air border, point 30 the gray/white matter border, point 40 is at ½ depth of the white matter. For the example of the healthy (d), at point 10 and 20 there are two small dips in signal intensity values for the histology. These reflect the lines of Baillarger. For the FTLD case (h), there is a sharp decrease in signal intensity starting from the first segments, reflecting diffuse iron accumulation.The signal intensity values are scaled for all three modalities with the minimum value set at 0 and the maximum value set at 1. The gray vertical dotted line depicts the border between gray matter and white matter. QSM is visualized with scale [−0.065:0.065]. GM: gray matter; QSM: quantitative susceptibility mapping; T2*-w MRI: T2*-weighted magnetic resonance imaging; WM: white matter. (For interpretation of the references to colour in this figure legend, the reader is referred to the web version of this article.)

intensity values in the deep cortical layers, corresponding to visible iron accumulation on T2*-w MRI and histology. On QSM, this iron accumulation is first visible as an increase in the signal intensity values, corresponding to an increased susceptibility at segment 10 until segment 20 and close to segment 30. At segment 30, there is a steep drop of signal intensity reflecting the U-fibers.

When looking at the average cortical layer profiles, the FTLD cases showed a lower average signal intensity value in the temporal cortex compared to the HC visible on the cortical layer profiles of the T2*-w MRI and histology and in the frontal cortex on the T2*-w MRI (Fig. 7). Around segment 5 of the cortical layer profile for the T2*-w MRI of the temporal cortex, there was a small dip of the values corresponding to the superficial hypointense band, followed by lower values for the deeper cortical layers from segment 10 onwards. The area between the curves was 2.57 ($p < 0.001$). In the frontal cortex, there is a lower overall signal intensity in the FTLD cases compared to HC. The area between the curves was 0.870 ($p = 0.038$). The average cortical layer profile in the temporal cortex on the histological slides showed a lower signal intensity value for the FTLD cases compared to the HC in the gray matter with a similar drop around the gray matter white/matter border at segment 30. The area between the curves was 2.17 ($p < 0.001$). The other cortical layer profiles had similar patterns between FTLD and HC ($p > 0.05$). The confidence interval of the cortical layer profiles in the QSM however showed a large variability in both cortices in FTLD, reflecting changes in susceptibility compared to HC.

3.5. Cortical layer profile correlation

There was a good mean correlation between the cortical layer profiles for histology and the T2*-w MRI ($r = 0.92$, $R^2 = 0.85$, $p < 0.001$) for the frontal cortex and ($r = 0.92$, $R^2 = 0.85$, $p < 0.001$) for the temporal cortex. There was a weak correlation between histology and QSM for both the frontal ($r = 0.41$, $R^2 = 0.17$, $p < 0.001$) and the temporal cortex ($r = 0.43$, $R^2 = 0.19$, $p < 0.001$) and for T2*-w MRI and QSM for both the frontal ($r = 0.40$, $R^2 = 0.16$, $p < 0.001$) and temporal cortex ($r = 0.44$, $R^2 = 0.19$, $p < 0.001$).

4. Discussion

In this study we demonstrated direct comparison of ex vivo ultra-high field T2*-w MRI, QSM, and histology for FTLD cases and healthy controls. An important and novel finding is that T2*-w MRI and QSM complement each other as they allow assessment of both paramagnetic (e.g., iron) and diamagnetic (e.g., myelin) contributions to the MRI contrasts. With QSM, we observed the presence of more pronounced subcortical U-fibers in the superficial white matter in FTLD cases compared to healthy controls. Additionally, we found more severe iron accumulation in FTLD cases compared to HC, displayed as an inhomogeneous cortex, diffuse hypointense mid cortical bands obscuring the normal cortical layering, and superficial hypointense bands in the gray matter on both histology and post-mortem MRI.

Our study builds on the pilot MRI findings of Giannini et al. (2023), providing a more comprehensive characterization of cortical iron-related changes on ultra-high field MRI. By adding quantitative cortical layer profiles and direct comparison of T2*-w MRI and QSM to histology, we extend previous descriptive observations of cortical iron bands toward a more detailed spatial and quantitative analysis. Furthermore, by including additional FTLD cases and healthy controls, we assess the strength of these features and explore the potential of QSM as a complementary technique to T2*-w MRI.

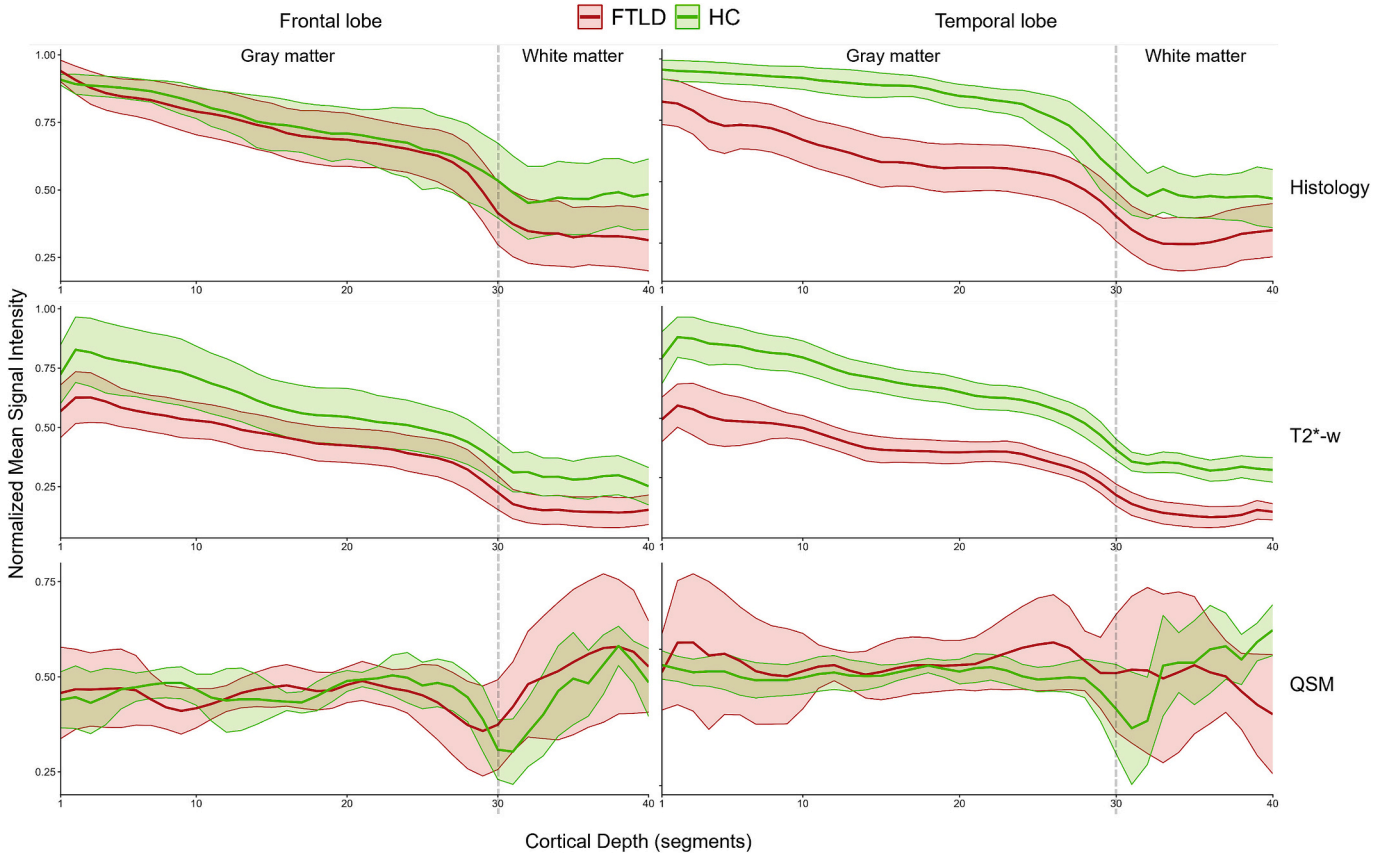

Fig. 7. Average mean scaled gray intensity value over the cortical depth per modality (rows) and region (columns) for the FTLD cases (red) and controls (green). The FTLD cases have lower mean signal intensity values for the temporal cortex on both histology and T2*-w MRI and in the frontal cortex for the T2*-w MRI, reflecting iron accumulation. Mean is plotted (line) with the 95% confidence interval (ribbon). Gray dotted line indicates the transition from GM to WM FTLD: Frontotemporal lobar degeneration; GM: gray matter; QSM: quantitative susceptibility mapping; T2*-w MRI: T2*-weighted magnetic resonance imaging; WM: white matter. (For interpretation of the references to colour in this figure legend, the reader is referred to the web version of this article.)

Our finding of increased iron load in FTLD is consistent with previous studies reporting iron accumulation across different FTLD subtypes (De Reuck et al., 2017; De Reuck et al., 2014; Giannini et al., 2023; Mazzucchi et al., 2019; Satoh et al., 2023; Sheelakumari et al., 2017). Iron accumulation was mainly located in the temporal cortex of the FTLD cases. This likely reflects the fact that four cases in our cohort presented with the semantic variant of PPA (svPPA) and five carried a *MAPT* mutation. In both instances, pathology is most prominent in the temporal lobes, especially during early disease stages (Boeve et al., 2005; Giannini et al., 2023; Gorno-Tempini et al., 2011; Planche et al., 2025; Poos et al., 2022; Sheelakumari et al., 2017; Staffaroni et al., 2022; Whitwell et al., 2009).

We observed no significant differences in iron accumulation between FTLD-tau and FTLD-TDP. This aligns with our previous pilot study of six cases and is consistent with Giannini et al. (2023), who focused exclusively on FTLD-TDP type B. In contrast, our results differ from those reported by Tisdall et al. (2022), who did find a distinction between FTLD-tau and FTLD-TDP. This discrepancy may be attributed to the inclusion of FTLD-TDP types A and C in their study; in these subtypes, pathology mainly affects the upper cortical layers. In type B, however, both upper and lower layers are affected, a pattern similar to that seen in FTLD-tau. A possible explanation for our lack of significant findings is the inclusion of all three FTLD-TDP subtypes in our cohort. Since these subgroups have small sample sizes and introduce pathological heterogeneity, they may have obscured statistical differences. However, one can appreciate the variety of patterns of iron accumulation across the cases in Supplementary Fig. A. 4. Future studies should focus on larger cohorts to determine whether differences exist not only between FTLD-tau and FTLD-TDP but also among the specific FTLD-TDP subtypes.

An interesting finding was the observation of prominent U-fibers. U-fibers are short connections between adjacent gyri within the same region of the brain and are involved in intergyral communication and higher cognitive functions (Catani et al., 2012; Nie et al., 2024). These fibers are the last to be myelinated, a process heavily dependent on iron. We observed more pronounced U-fibers in the frontal cortex, evident on histology and QSM, in both FTLD-tau and FTLD-TDP. Especially in the cortical layer profiles of the QSM maps, an overall increase in the susceptibility and a larger 95% confidence interval at segment 30 of FTLD cases compared to HC is markedly visible. This overall increased susceptibility could be attributed to demyelination or iron accumulation (Wisnieff et al., 2015). However, further investigation with specific histological myelin staining or chi-separation (Shin et al., 2021) to disentangle intra-voxel paramagnetic and diamagnetic contributions, is necessary to make a definitive conclusion. This phenomenon of affected superficial white matter and U-fibers was also observed in FTLD in a postmortem study (Tisdall et al., 2022) and in an in vivo MRI study, in which degeneration of these short-range U-fibers was linked to semantic dysfunction (Savard et al., 2022). Future in vivo studies could combine diffusion tensor imaging (DTI) or diffusion-weighted imaging (DWI) with QSM to investigate this phenomenon more comprehensively.

The cortical layer profiles of the FTLD cases in the temporal cortex on histology and T2*-w MRI and in the frontal cortex on the T2*-w MRI showed a different pattern compared to HC, with lower signal intensity values reflecting iron accumulation, in line with qualitative visual observations. The cortical layer profiles offer the advantage of providing a quantitative assessment of iron accumulation across the cortical depth in

a prespecified position, in contrast to the more subjective visual rating scores which are subject to interrater variability. The cortical layer profiles of T2*-w MRI and histology showed a good correlation for both brain regions, suggesting that T2*-w MRI accurately reflects similar patterns of iron accumulation seen with histology, such as the diffuse mid cortical band in the temporal cortices. As we adjusted for staining differences in the histological data by applying a manual selected window, we expected the profiles of the histological data in the white matter to overlap. This was not the case, most likely because the normalization was based on all visible white matter, whereas the line profiles only included part of the white matter in the gyri, which tended to show more intense staining. The cortical layer profiles extracted from the QSM maps showed a different overall pattern compared to the histological and T2*-w data, reflected by the low correlation coefficients and the relatively flat line. This could be attributed to the display and interpretation of the signal intensity values in the image and the orientation of the tissue block in respect to the main magnetic field. A QSM image displays changes in susceptibility compared to a reference. In our cortical layer profiles, the lines were relatively flat, centered around the middle (reference), with the changes in susceptibility shown as an increased or decreased signal intensity relative to the reference, depending on the orientation of the tissue bock. If you take then the group average of these results, you effectively cancel out the two directions of the changes, resulting in a relatively flat line. Therefore, to assess patterns of iron accumulation, it would be more appropriate to compare the 95% confidence interval than the area between the curves.

QSM reflects the combined influence of iron, myelin, and tissue orientation relative to the main magnetic field on local magnetic susceptibility. While QSM showed weaker correlation with histology and T2*-w MRI, it provides unique quantitative information. QSM contrast shows the dominant susceptibility at each voxel, with paramagnetic components such as iron appear hyperintense (white), whereas diamagnetic components such as myelin appear hypointense (black). The apparent susceptibility of white matter is known to depend on the orientation of its anisotropic fiber structure with respect to the magnetic field, which may result in either hyperintense or hypointense contrast (Wharton and Bowtell, 2015). In contrast, gray matter is generally considered isotropic and therefore expected to exhibit susceptibility values independent of field orientation. However, this assumption does not hold at the high spatial resolution employed in the present study. At this scale, highly myelinated features such as the lines of Baillarger in the deep cortical layers become discernible, and even paramagnetic substances may line up anisotropically (Chen et al., 2025). As we selected the line profiles in the middle of a gyrus, and gyri were orientated variable with respect to the main magnetic field depending on the anatomy of the tissue block, some U-fibers depicted as white, and others as black, effectively cancelling out their strong susceptibility profile in the mean cortical layer profile. The challenges in QSM processing, such as erosion of tissue borders and orientation dependence, are important limitations. However, QSM's ability to quantify susceptibility and its potential to disentangle iron and myelin contribution when combined with advanced post-processing or multi-modal imaging protocols, makes it a valuable tool for to study changes in microstructure. Future studies should optimize QSM reconstruction for small tissue blocks and explore advanced techniques such as chi-separation (Shin et al., 2021) to improve specificity for iron.

QSM and T2*-w MRI seem to be complementary to each other. Based on the susceptibility source (iron and/or myelin) and the scale of these sources, features such as intracellular iron deposition or highly organized fiber bundles are emphasized. Both scans are based on the same relatively straightforward MGE sequence, if acquired with multiple echoes. However, while the T2*-w MRI scan requires no additional processing, QSM involves a more extensive post-processing pipeline. Nevertheless, most vendors nowadays offer the pipeline integrated in the system (Boehm et al., 2022; Voon et al., 2025) and a consensus paper from the community with guidelines has been published (Bilgic et al., 2024), and thus analysis of both contrasts in conjunction would in practice always be possible. T2*-w MRI provides high anatomical resolution and is more sensitive to sub-voxel susceptibility sources which are visible due to the blooming effect. However, T2*-w MRI cannot separate sources of contrast. On the other hand, QSM can separate contrasts and is sensitive to microstructural tissue orientation, as seen in the U-fibers, but its processing can introduce blurring and edge erosion. In practice, the choice between T2*-w MRI and QSM depends on the specific feature of interest.

One of the strengths of this study is that we used the same tissue block for both the MRI and the histological analyses, enabling direct comparison and validation across the three modalities. Moreover, the cortical layer profiles provided a more detailed visualization of spatial patterns of iron accumulations. On the other hand, as HC data were reused from a previous study (Bulk et al., 2018b), the MRI protocol was slightly different from the FTLD cases. The TR for the FTLD and HC scans was not the same. However, since the T1 for gray matter and white matter converges after fixation and is severely shortened (Raman et al., 2017), we do not expect differences in T1-weighting between the two protocols. To compare the T2*-w MRI contrasts, we matched the TE for the FTLD cases as close as possible to that of the HC. In addition, the FTLD sample was both small and heterogeneous with different pathologies and clinical diagnosis. This is, however, inherent to postmortem studies in a rare disorder. It is advised that the results are further verified in a larger sample size.

In conclusion, this study demonstrates that both T2*-w MRI and QSM can detect pathological iron accumulation in FTLD, with T2*-w MRI showing strongest correspondence to histology. However, QSM provides complementary quantitative information and may be particularly valuable for assessing U-fiber involvement. While our findings are based on ex vivo data at a microscopic scale, the translation to in vivo clinical practice is promising. Although the resolution will shift to a macroscopic scale focusing on general brain regions rather than fine microstructural details, similar approaches have already shown potential in Parkinson's disease (Langkammer et al., 2016), Alzheimer's disease (Acosta-Cabronero et al., 2013), and Amyotrophic Lateral Sclerosis studies (Acosta-Cabronero et al., 2018). Together, these findings support the potential of MRI-based iron mapping as a biomarker for FTLD. We are currently running an in vivo study in a larger FTLD cohort using 7 T T2*-w MRI and QSM to validate these findings and further evaluate their prognostic potential (Prinse et al., 2025).

CRediT authorship contribution statement

Fieke A.M. Prinse: Writing – original draft, Visualization, Validation, Project administration, Methodology, Investigation, Formal analysis, Data curation, Conceptualization. **Elise G.P. Dopper:** Writing – review & editing, Supervision. **Lucia A.A. Giannini:** Writing – review & editing. **Marjolein Bulk:** Writing – review & editing, Project administration, Funding acquisition, Data curation, Conceptualization. **Ernst Suidgeest:** Writing – review & editing, Data curation. **Kyra Dijkstra:** Writing – review & editing, Data curation. **Renee van Buuren:** Writing – review & editing, Data curation. **Jelle J. Goeman:** Writing – review & editing, Formal analysis. **Niels Dekker:** Writing – review & editing, Formal analysis. **Marius Staring:** Writing – review & editing, Formal analysis. **Chloé Najac:** Writing – review & editing, Supervision. **John C. van Swieten:** Writing – review & editing, Supervision, Conceptualization. **Harro Seelaar:** Writing – review & editing, Supervision, Project administration, Funding acquisition, Conceptualization. **Louise van der Weerd:** Writing – review & editing, Supervision, Project administration, Conceptualization.

Ethics statement

Study procedures were performed in accordance with Dutch ethical guidelines (Code for Proper Secondary Use of Human Tissue, Dutch

Federation of Medical Scientific Societies). Approval by an ethical committee was not required for the performance of this study, which used de-anonymized brain bank tissue samples. Informed consent for brain donation and scientific use was obtained prior to death.

Declaration of competing interest

The authors declare that they have no known competing financial interests or personal relationships that could have appeared to influence the work reported in this paper.

Acknowledgments

We thank all patients and their families for making this research possible. We thank Linda van der Graaf for her help with the data acquisition. This work was supported by a personal grant (M. Bulk) from Alzheimer Nederland (Call for Biomedical Research WE.03-2020-10) and a personal grant (H. Seelaar) from ZonMW-Alzheimer Nederland (Memorabel Research Fellowship 2019: project 733050513). Two of the authors of this publication are members of the European Reference Network for Rare Neurological Diseases - Project ID No 739510.

Appendix A. Supplementary data

Supplementary data to this article can be found online at https://doi.org/10.1016/j.nbd.2026.107461.

Data availability

Data will be made available on request.

References

Acosta-Cabronero, J., Williams, G.B., Cardenas-Blanco, A., Arnold, R.J., Lupson, V., Nestor, P.J., 2013. In vivo quantitative susceptibility mapping (QSM) in Alzheimer's disease. PLoS One 8, e81093.

Acosta-Cabronero, J., Machts, J., Schreiber, S., Abdulla, S., Kollewe, K., Petri, S., Spotorno, N., Kaufmann, J., Heinze, H.J., Dengler, R., Vielhaber, S., Nestor, P.J., 2018. Quantitative Susceptibility MRI to Detect Brain Iron in Amyotrophic Lateral Sclerosis. Radiology 289, 195–203.

Ayton, S., Moreau, C., Devos, D., Bush, A.I., 2025. Iron on trial: recasting the role of iron in neurodegeneration. Brain 148 (12), 4241–4247.

Baker, M., Mackenzie, I.R., Pickering-Brown, S.M., Gass, J., Rademakers, R., Lindholm, C., Snowden, J., Adamson, J., Sadovnick, A.D., Rollinson, S., Cannon, A., Dwosh, E., Neary, D., Melquist, S., Richardson, A., Dickson, D., Berger, Z., Eriksen, J., Robinson, T., Zehr, C., Dickey, C.A., Crook, R., McGowan, E., Mann, D., Boeve, B., Feldman, H., Hutton, M., 2006. Mutations in progranulin cause tau-negative frontotemporal dementia linked to chromosome 17. Nature 442, 916–919.

Bilgic, B., Costagli, M., Chan, K.S., Duyn, J., Langkammer, C., Lee, J., Li, X., Liu, C., Marques, J.P., Milovic, C., Robinson, S.D., Schweser, F., Shmueli, K., Spincemaille, P., Straub, S., van Zijl, P., Wang, Y., 2024. Recommended implementation of quantitative susceptibility mapping for clinical research in the brain: a consensus of the ISMRM electro-magnetic tissue properties study group. Magn. Reson. Med. 91, 1834–1862.

Boehm, C., Sollmann, N., Meineke, J., Ruschke, S., Dieckmeyer, M., Weiss, K., Zimmer, C., Makowski, M.R., Baum, T., Karampinos, D.C., 2022. Preconditioned water-fat total field inversion: application to spine quantitative susceptibility mapping. Magn. Reson. Med. 87, 417–430.

Boeve, B.F., Tremont-Lukats, I.W., Waclawik, A.J., Murrell, J.R., Hermann, B., Jack Jr., C.R., Shiung, M.M., Smith, G.E., Nair, A.R., Lindor, N., Koppikar, V., Ghetti, B., 2005. Longitudinal characterization of two siblings with frontotemporal dementia and parkinsonism linked to chromosome 17 associated with the S305N tau mutation. Brain 128, 752–772.

Bulk, M., Abdelmoula, W.M., Nabuurs, R.J.A., van der Graaf, L.M., Mulders, C.W.H., Mulder, A.A., Jost, C.R., Koster, A.J., van Buchem, M.A., Natté, R., Dijkstra, J., van der Weerd, L., 2018a. Postmortem MRI and histology demonstrate differential iron accumulation and cortical myelin organization in early- and late-onset Alzheimer's disease. Neurobiol. Aging 62, 231–242.

Bulk, M., Kenkhuis, B., van der Graaf, L.M., Goeman, J.J., Natte, R., van der Weerd, L., 2018b. Postmortem T2*- Weighted MRI Imaging of Cortical Iron Reflects Severity of Alzheimer's Disease. J. Alzheimer's Dis 65, 1125–1137.

Bulk, M., Hegeman-Kleinn, I., Kenkhuis, B., Suidgeest, E., van Roon-Mom, W., Lewerenz, J., van Duinen, S., Ronen, I., van der Weerd, L., 2020. Pathological characterization of T2*-weighted MRI contrast in the striatum of Huntington's disease patients. Neuroimage Clin. 28, 102498.

Catani, M., Dell'Acqua, F., Vergani, F., Malik, F., Hodge, H., Roy, P., Valabregue, R., Thiebaut de Schotten, M., 2012. Short frontal lobe connections of the human brain. Cortex 48, 273–291.

Chan, K.-S., Marques, J.P., 2021. SEPIA—Susceptibility mapping pipeline tool for phase images. NeuroImage 227, 117611.

Chen, J., Gkotsoulias, D.G., Jaffe, J.E., Gräßle, T., Jäger, C., Goné Bi, Z.B., Crockford, C., Wittig, R., Möller, H.E., Liu, C., 2025. Observations of anisotropic paramagnetic and diamagnetic susceptibility in the primate brain. bioRxiv, 2025.2011.2021.689628.

Cruts, M., Gijselinck, I., van der Zee, J., Engelborghs, S., Wils, H., Pirici, D., Rademakers, R., Vandenberghe, R., Dermaut, B., Martin, J.J., van Duijn, C., Peeters, K., Sciot, R., Santens, P., De Pooter, T., Mattheijssens, M., Van den Broeck, M., Cuijt, I., Vennekens, K., De Deyn, P.P., Kumar-Singh, S., Van Broeckhoven, C., 2006. Null mutations in progranulin cause ubiquitin-positive frontotemporal dementia linked to chromosome 17q21. Nature 442, 920–924.

De Reuck, J., Devos, D., Moreau, C., Auger, F., Durieux, N., Deramecourt, V., Pasquier, F., Maurage, C.A., Cordonnier, C., Leys, D., Bordet, R., 2017. Topographic distribution of brain iron deposition and small cerebrovascular lesions in amyotrophic lateral sclerosis and in frontotemporal lobar degeneration: a post-mortem 7.0-tesla magnetic resonance imaging study with neuropathological correlates. Acta Neurol. Belg. 117, 873–878.

De Reuck, J.L., Deramecourt, V., Auger, F., Durieux, N., Cordonnier, C., Devos, D., Defebvre, L., Moreau, C., Caparros-Lefebvre, D., Leys, D., Maurage, C.A., Pasquier, F., Bordet, R., 2014. Iron deposits in post-mortem brains of patients with neurodegenerative and cerebrovascular diseases: a semi-quantitative 7.0 T magnetic resonance imaging study. Eur. J. Neurol. 21, 1026–1031.

DeJesus-Hernandez, M., Mackenzie, I.R., Boeve, B.F., Boxer, A.L., Baker, M., Rutherford, N.J., Nicholson, A.M., Finch, N.A., Flynn, H., Adamson, J., Kouri, N., Wojtas, A., Sengdy, P., Hsiung, G.Y., Karydas, A., Seeley, W.W., Josephs, K.A., Coppola, G., Geschwind, D.H., Wszolek, Z.K., Feldman, H., Knopman, D.S., Petersen, R.C., Miller, B.L., Dickson, D.W., Boylan, K.B., Graff-Radford, N.R., Rademakers, R., 2011. Expanded GGGGCC hexanucleotide repeat in noncoding region of C9ORF72 causes chromosome 9p-linked FTD and ALS. Neuron 72, 245–256.

van Duijn, S., Nabuurs, R.J., van Rooden, S., Maat-Schieman, M.L., van Duinen, S.G., van Buchem, M.A., van der Weerd, L., Natté, R., 2011. MRI artifacts in human brain tissue after prolonged formalin storage. Magn. Reson. Med. 65, 1750–1758.

Dusek, P., Hofer, T., Alexander, J., Roos, P.M., Aaseth, J.O., 2022. Cerebral Iron Deposition in Neurodegeneration. Biomolecules 12.

Ferretti, S., Zanella, I., 2024. The underestimated role of iron in frontotemporal dementia: a narrative review. Int. J. Mol. Sci. 25.

Giannini, L.A.A., Bulk, M., Kenkhuis, B., Rajicic, A., Melhem, S., Hegeman-Kleinn, I., Bossoni, L., Suidgeest, E., Dopper, E.G.P., van Swieten, J.C., van der Weerd, L., Seelaar, H., 2023. Cortical iron accumulation in MAPT- and C9orf72-associated frontotemporal lobar degeneration. Brain Pathol. 33, e13158.

Goeman, J.J., De Jong, N.H., 2018. How well does the sum score summarize the test? Summability as a measure of internal consistency. Educ. Meas. Issues Pract. 37, 54–63.

Goeman, J.J., Solari, A., 2022. Comparing three groups. Am. Stat. 76, 168–176.

Gorno-Tempini, M.L., Hillis, A.E., Weintraub, S., Kertesz, A., Mendez, M., Cappa, S.F., Ogar, J.M., Rohrer, J.D., Black, S., Boeve, B.F., Manes, F., Dronkers, N.F., Vandenberghe, R., Rascovsky, K., Patterson, K., Miller, B.L., Knopman, D.S., Hodges, J.R., Mesulam, M.M., Grossman, M., 2011. Classification of primary progressive aphasia and its variants. Neurology 76, 1006–1014.

Grossman, M., Seeley, W.W., Boxer, A.L., Hillis, A.E., Knopman, D.S., Ljubenov, P.A., Miller, B., Piguet, O., Rademakers, R., Whitwell, J.L., Zetterberg, H., van Swieten, J. C., 2023. Frontotemporal lobar degeneration. Nat. Rev. Dis. Primers 9, 40.

Hutton, M., Lendon, C.L., Rizzu, P., Baker, M., Froelich, S., Houlden, H., Pickering-Brown, S., Chakraverty, S., Isaacs, A., Grover, A., Hackett, J., Adamson, J., Lincoln, S., Dickson, D., Davies, P., Petersen, R.C., Stevens, M., de Graaff, E., Wauters, E., van Baren, J., Hillebrand, M., Joosse, M., Kwon, J.M., Nowotny, P., Che, L.K., Norton, J., Morris, J.C., Reed, L.A., Trojanowski, J., Basun, H., Lannfelt, L., Neystat, M., Fahn, S., Dark, F., Tannenberg, T., Dodd, P.R., Hayward, N., Kwok, J.B., Schofield, P.R., Andreadis, A., Snowden, J., Craufurd, D., Neary, D., Owen, F., Oostra, B.A., Hardy, J., Goate, A., van Swieten, J., Mann, D., Lynch, T., Heutink, P., 1998. Association of missense and 5′-splice-site mutations in tau with the inherited dementia FTDP-17. Nature 393, 702–705.

Langkammer, C., Pirpamer, L., Seiler, S., Deistung, A., Schweser, F., Franthal, S., Homayoon, N., Katschnig-Winter, P., Koegl-Wallner, M., Pendl, T., Stoegerer, E.M., Wenzel, K., Fazekas, F., Ropele, S., Reichenbach, J.R., Schmidt, R., Schwingenschuh, P., 2016. Quantitative Susceptibility Mapping in Parkinson's Disease. PLoS One 11, e0162460.

Langkammer, C., Schweser, F., Shmueli, K., Kames, C., Li, X., Guo, L., Milovic, C., Kim, J., Wei, H., Bredies, K., Buch, S., Guo, Y., Liu, Z., Meineke, J., Rauscher, A., Marques, J. P., Bilgic, B., 2018. Quantitative susceptibility mapping: report from the 2016 reconstruction challenge. Magn. Reson. Med. 79, 1661–1673.

Lee, S., Martinez-Valbuena, I., de Andrea, C.E., Villalba-Esparza, M., Ilaalagan, S., Couto, B., Visanji, N.P., Lang, A.E., Kovacs, G.G., 2023. Cell-specific dysregulation of iron and oxygen homeostasis as a novel pathophysiology in PSP. Ann. Neurol. 93, 431–445.

Lee, S.H., Lyoo, C.H., Ahn, S.J., Rinne, J.O., Lee, M.S., 2017. Brain regional iron contents in progressive supranuclear palsy. Parkinsonism Relat. Disord. 45, 28–32.

Li, W., Wu, B., Liu, C., 2011. Quantitative susceptibility mapping of human brain reflects spatial variation in tissue composition. Neuroimage 55, 1645–1656.

Liu, J., Liu, T., de Rochefort, L., Ledoux, J., Khalidov, I., Chen, W., Tsiouris, A.J., Wisnieff, C., Spincemaille, P., Prince, M.R., Wang, Y., 2012. Morphology enabled dipole inversion for quantitative susceptibility mapping using structural consistency

between the magnitude image and the susceptibility map. Neuroimage 59, 2560–2568.
Liu, T., Liu, J., de Rochefort, L., Spincemaille, P., Khalidov, I., Ledoux, J.R., Wang, Y., 2011. Morphology enabled dipole inversion (MEDI) from a single-angle acquisition: comparison with COSMOS in human brain imaging. Magn. Reson. Med. 66, 777–783.
Liu, Z., Spincemaille, P., Yao, Y., Zhang, Y., Wang, Y., 2018. MEDI+0: Morphology enabled dipole inversion with automatic uniform cerebrospinal fluid zero reference for quantitative susceptibility mapping. Magn. Reson. Med. 79, 2795–2803.
Mazzucchi, S., Frosini, D., Costagli, M., Del Prete, E., Donatelli, G., Cecchi, P., Migaleddu, G., Bonuccelli, U., Ceravolo, R., Cosottini, M., 2019. Quantitative susceptibility mapping in atypical Parkinsonisms. Neuroimage Clin. 24, 101999.
Nie, X., Ruan, J., Otaduy, M.C.G., Grinberg, L.T., Ringman, J., Shi, Y., 2024. Surface-based probabilistic fiber tracking in superficial white matter. IEEE Trans. Med. Imaging 43 (3), 1113–1124.
Ntatsis, K., N.D, Valk, V., Birdsong, T., Zukić, D., Klein, S., Staring, M., McCormick, M., 2023. itk-elastix: Medical image registration in Python. In: 22nd Python in Science Conference, pp. 101–105.
Pérez, M., Valpuesta, J.M., de Garcini, E.M., Quintana, C., Arrasate, M., López Carrascosa, J.L., Rábano, A., García de Yébenes, J., Avila, J., 1998. Ferritin is associated with the aberrant tau filaments present in progressive supranuclear palsy. Am. J. Pathol. 152, 1531–1539.
Planche, V., Mansencal, B., Fonov, V., Manjon, J.V., Tourdias, T., Bouzigues, A., Russell, L.L., Foster, P.H., Ferry-Bolder, E., van Swieten, J.C., Jiskoot, L.C., Seelaar, H., Sanchez-Valle, R., Laforce, R., Graff, C., Galimberti, D., Vandenberghe, R., de Mendonça, A., Tiraboschi, P., Santana, I., Gerhard, A., Levin, J., Sorbi, S., Otto, M., Bertoux, M., Lebouvier, T., Butler, C.R., Le Ber, I., Finger, E., Tartaglia, M.C., Masellis, M., Rowe, J.B., Synofzik, M., Moreno, F., Borroni, B., Rohrer, J.D., Collins, D.L., Ducharme, S., Coupé, P., 2025. Anatomical progression of genetic frontotemporal lobar degeneration across the lifespan. Brain 148, 3880–3892.
Poos, J.M., Grandpierre, L.D.M., van der Ende, E.L., Panman, J.L., Papma, J.M., Seelaar, H., van den Berg, E., van't Klooster, R., Bron, E., Steketee, R., Vernooij, M. W., Pijnenburg, Y.A.L., Rombouts, S., van Swieten, J., Jiskoot, L.C., 2022. Longitudinal brain atrophy rates in presymptomatic carriers of genetic frontotemporal dementia. Neurology 99, e2661–e2671.
Prinse, F.A.M., van der Weerd, L., van Swieten, J.C., Ronen, I., Seelaar, H., Hirschler, L., Najac, C., Dopper, E.G.P., 2025. Investigating the role of neuroinflammation and brain clearance in frontotemporal lobar degeneration using 7T MRI and fluid biomarkers: protocol for a cross-sectional study in a tertiary care setting. BMJ Open 15, e102668.
Raman, M.R., Shu, Y., Lesnick, T.G., Jack, C.R., Kantarci, K., 2017. Regional T(1) relaxation time constants in Ex vivo human brain: longitudinal effects of formalin exposure. Magn. Reson. Med. 77, 774–778.
Renton, A.E., Majounie, E., Waite, A., Simon-Sanchez, J., Rollinson, S., Gibbs, J.R., Schymick, J.C., Laaksovirta, H., van Swieten, J.C., Myllykangas, L., Kalimo, H., Paetau, A., Abramzon, Y., Remes, A.M., Kaganovich, A., Scholz, S.W., Duckworth, J., Ding, J., Harmer, D.W., Hernandez, D.G., Johnson, J.O., Mok, K., Ryten, M., Trabzuni, D., Guerreiro, R.J., Orrell, R.W., Neal, J., Murray, A., Pearson, J., Jansen, I. E., Sondervan, D., Seelaar, H., Blake, D., Young, K., Halliwell, N., Callister, J.B., Toulson, G., Richardson, A., Gerhard, A., Snowden, J., Mann, D., Neary, D., Nalls, M. A., Peuralinna, T., Jansson, L., Isoviita, V.M., Kaivorinne, A.L., Holtta-Vuori, M., Ikonen, E., Sulkava, R., Benatar, M., Wuu, J., Chio, A., Restagno, G., Borghero, G., Sabatelli, M., Consortium, I., Heckerman, D., Rogaeva, E., Zinman, L., Rothstein, J. D., Sendtner, M., Drepper, C., Eichler, E.E., Alkan, C., Abdullaev, Z., Pack, S.D., Dutra, A., Pak, E., Hardy, J., Singleton, A., Williams, N.M., Heutink, P., Pickering-Brown, S., Morris, H.R., Tienari, P.J., Traynor, B.J., 2011. A hexanucleotide repeat expansion in C9ORF72 is the cause of chromosome 9p21-linked ALS-FTD. Neuron 72, 257–268.
Robinson, S.D., Bredies, K., Khabipova, D., Dymerska, B., Marques, J.P., Schweser, F., 2017. An illustrated comparison of processing methods for MR phase imaging and QSM: combining array coil signals and phase unwrapping. NMR Biomed. 30.
Satoh, R., Weigand, S.D., Pham, N.T.T., Ali, F., Arani, A., Senjem, M.L., Jack Jr., C.R., Whitwell, J.L., Josephs, K.A., 2023. Magnetic Susceptibility in Progressive Supranuclear Palsy Variants, Parkinson's Disease, and Corticobasal Syndrome. Mov. Disord. 38, 2282–2290.
Savard, M., Pascoal, T.A., Servaes, S., Dhollander, T., Iturria-Medina, Y., Kang, M.S., Vitali, P., Therriault, J., Mathotaarachchi, S., Benedet, A.L., Gauthier, S., Rosa-Neto, P., 2022. Impact of long- and short-range fibre depletion on the cognitive deficits of fronto-temporal dementia. eLife 11.
Schindelin, J., Arganda-Carreras, I., Frise, E., Kaynig, V., Longair, M., Pietzsch, T., Preibisch, S., Rueden, C., Saalfeld, S., Schmid, B., Tinevez, J.Y., White, D.J., Hartenstein, V., Eliceiri, K., Tomancak, P., Cardona, A., 2012. Fiji: an open-source platform for biological-image analysis. Nat. Methods 9, 676–682.
Schofield, M.A., Zhu, Y., 2003. Fast phase unwrapping algorithm for interferometric applications. Opt. Lett. 28, 1194–1196.
Shamonin, D.P., Bron, E.E., Lelieveldt, B.P., Smits, M., Klein, S., Staring, M., 2013. Fast parallel image registration on CPU and GPU for diagnostic classification of Alzheimer's disease. Front. Neuroinform. 7, 50.
Sheelakumari, R., Kesavadas, C., Varghese, T., Sreedharan, R.M., Thomas, B., Verghese, J., Mathuranath, P.S., 2017. Assessment of Iron Deposition in the Brain in Frontotemporal Dementia and Its Correlation with Behavioral Traits. AJNR Am. J. Neuroradiol. 38, 1953–1958.
Shin, H.-G., Lee, J., Yun, Y.H., Yoo, S.H., Jang, J., Oh, S.-H., Nam, Y., Jung, S., Kim, S., Fukunaga, M., Kim, W., Choi, H.J., Lee, J., 2021. χ-separation: Magnetic susceptibility source separation toward iron and myelin mapping in the brain. NeuroImage 240, 118371.
Smith, S.M., 2002. Fast robust automated brain extraction. Hum. Brain Mapp. 17, 143–155.
Staffaroni, A.M., Quintana, M., Wendelberger, B., Heuer, H.W., Russell, L.L., Cobigo, Y., Wolf, A., Goh, S.M., Petrucelli, L., Gendron, T.F., Heller, C., Clark, A.L., Taylor, J.C., Wise, A., Ong, E., Forsberg, L., Brushaber, D., Rojas, J.C., VandeVrede, L., Ljubenkov, P., Kramer, J., Casaletto, K.B., Appleby, B., Bordelon, Y., Botha, H., Dickerson, B.C., Domoto-Reilly, K., Fields, J.A., Foroud, T., Gavrilova, R., Geschwind, D., Ghoshal, N., Goldman, J., Graff-Radford, J., Graff-Radford, N., Grossman, M., Hall, M.G.H., Hsiung, G.Y., Huey, E.D., Irwin, D., Jones, D.T., Kantarci, K., Kaufer, D., Knopman, D., Kremers, W., Lago, A.L., Lapid, M.I., Litvan, I., Lucente, D., Mackenzie, I.R., Mendez, M.F., Mester, C., Miller, B.L., Onyike, C.U., Rademakers, R., Ramanan, V.K., Ramos, E.M., Rao, M., Rascovsky, K., Rankin, K.P., Roberson, E.D., Savica, R., Tartaglia, M.C., Weintraub, S., Wong, B., Cash, D.M., Bouzigues, A., Swift, I.J., Peakman, G., Bocchetta, M., Todd, E.G., Convery, R.S., Rowe, J.B., Borroni, B., Galimberti, D., Tiraboschi, P., Masellis, M., Finger, E., van Swieten, J.C., Seelaar, H., Jiskoot, L.C., Sorbi, S., Butler, C.R., Graff, C., Gerhard, A., Langheinrich, T., Laforce, R., Sanchez-Valle, R., de Mendonça, A., Moreno, F., Synofzik, M., Vandenberghe, R., Ducharme, S., Le Ber, I., Levin, J., Danek, A., Otto, M., Pasquier, F., Santana, I., Kornak, J., Boeve, B.F., Rosen, H.J., Rohrer, J.D., Boxer, A.L., 2022. Temporal order of clinical and biomarker changes in familial frontotemporal dementia. Nat. Med. 28, 2194–2206.
Tisdall, M.D., Ohm, D.T., Lobrovich, R., Das, S.R., Mizsei, G., Prabhakaran, K., Ittyerah, R., Lim, S., McMillan, C.T., Wolk, D.A., Gee, J., Trojanowski, J.Q., Lee, E.B., Detre, J.A., Yushkevich, P., Grossman, M., Irwin, D.J., 2022. Ex vivo MRI and histopathology detect novel iron-rich cortical inflammation in frontotemporal lobar degeneration with tau versus TDP-43 pathology. Neuroimage Clin. 33, 102913.
Voon, C.C., Meineke, J., Wiltgen, T., McGinnis, J., Berg, R., Preibisch, C., Schlaeger, S., Wiestler, B., Engl, C., Berthele, A., Kirschke, J.S., Hemmer, B., Mühlau, M., 2025. Quantitative susceptibility mapping of deep grey matter in MS: association with clinical scores and brain volume measures. Brain Behav. 15, e70988.
Wharton, S., Bowtell, R., 2015. Effects of white matter microstructure on phase and susceptibility maps. Magn. Reson. Med. 73, 1258–1269.
Whitwell, J.L., Jack Jr., C.R., Boeve, B.F., Senjem, M.L., Baker, M., Ivnik, R.J., Knopman, D.S., Wszolek, Z.K., Petersen, R.C., Rademakers, R., Josephs, K.A., 2009. Atrophy patterns in IVS10+16, IVS10+3, N279K, S305N, P301L, and V337M MAPT mutations. Neurology 73, 1058–1065.
Wisnieff, C., Ramanan, S., Olesik, J., Gauthier, S., Wang, Y., Pitt, D., 2015. Quantitative susceptibility mapping (QSM) of white matter multiple sclerosis lesions: Interpreting positive susceptibility and the presence of iron. Magn. Reson. Med. 74, 564–570.

Glossary

AD Alzheimer's disease:
ALS amyotrophic lateralsclerosis:
BET brain extraction tool:
bvFTD behavioral variant frontotemporal dementia:
CBS corticobasal syndrome:
CSF cerebrospinal fluid:
C9orf72-HRE chromosome 9 open reading frame 72 hexanucleotide repeat expansion:
DWI diffusion weighted imaging:
DTI diffusion tensor imaging:
FOV field of view:
FTLD frontotemporal lobar degeneration:
GRN progranulin:
HC healthy controls:
MAPT microtubule associated protein tau:
MGE multiple gradient echo:
PBS phosphate buffered saline:
PD Parkinson's disease:
PPA primary progressive aphasia:
PSP progressive supranuclear palsy:
QSM quantitative susceptibility mapping:
SWI susceptibility weighted imaging:
tau tubulin associated unit:
TDP-43 TAR DNA binding protein 43:
T2-w* T2*-weighted: